

Article

Development of Nanosized Mn₃O₄-Co₃O₄ on Multiwalled Carbon Nanotubes for Cathode Catalyst in Urea Fuel Cell

Thi Ngoc Tuyen Pham and Young Soo Yoon *

Department of Materials Science and Engineering, Gachon University, Bokjung-dong, Seongnam-si 1342, Korea; ngoctuyen1593@gmail.com

* Correspondence: benedicto@gachon.ac.kr; Tel.: +82-31-750-7015; Fax: +82-31-750-8988

Received: 30 March 2020; Accepted: 30 April 2020; Published: 7 May 2020

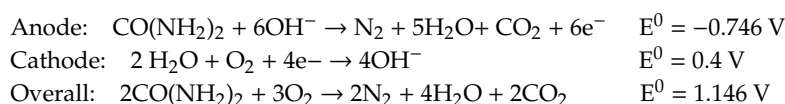


Abstract: Double-oxide Mn₃O₄-Co₃O₄ nanoparticles were synthesized and anchored on multiwalled carbon nanotubes (MWCNTs) via a single-step solvothermal method. The largest specific area (99.82 m²g⁻¹) of the catalyst was confirmed via a nitrogen adsorption isotherm. Furthermore, the uniform coating of the Mn₃O₄-Co₃O₄ nanoparticles on the surface of the MWCNTs was observed via scanning electron microscopy and transmission electron microscopy; the uniform coating provided an effective transport pathway during the electrocatalytic activities. The rotating disk electrode and rotating ring disk electrode measurements indicated that the electron transfer number was 3.96 and the evolution of H₂O₂ was 2%. In addition, the Mn₃O₄-Co₃O₄/MWCNT catalyst did not undergo urea poisoning and remained stable in an alkaline solution. Conversely, commercial Pt/C could not withstand urea poisoning for long. The performance cell achieved a power density of 0.4226 mW cm⁻² at 50 °C. Therefore, Mn₃O₄-Co₃O₄/MWCNT is an efficient and inexpensive noble-metal-free cathodic catalyst for direct urea fuel cells.

Keywords: urea fuel cell; cathode catalyst; oxygen reduction reaction

1. Introduction

In recent years, the demand for renewable energy has been gradually increasing. As a type of renewable energy carrier, urea is considered as a hydrogen carrier form because it is non-flammable, non-toxic, biodegradable, and abundant. Urea can be utilized as a power source with direct urea fuel cells (DUFCs). DUFCs represent novel technology for the efficient generation of electricity because of their numerous advantages, such as low cost, high energy-storage densities, and high levels of safety [1]. In addition, DUFCs generate electricity without releasing toxic products, thus limiting the level of environmental pollution. Hence, it constitutes an attractive power generation technology [2]. Furthermore, urea is widely available in industrial wastewater and human/animal urine. However, untreated urea could pose danger to both human health and the environment because it can hydrolyze into toxic ammonia and nitrite [3,4]. Therefore, DUFCs have two-fold benefits—they can generate electricity and produce clean water. In a DUFC, a urea electrooxidation reaction and oxygen reduction reaction (ORR) occur at the interface of the electrolyte and the electrocatalytic layers, and are expressed as follows [5]:



Lan et al. reported the first DUFC, which achieved a maximum power density of 1.7 mW cm^{-2} using a 1 M urea solution as the fuel [6]. Although the performance of DUFCs has been significantly improved, it is still lower than that of other fuel cells in terms of the current density. A major issue is the occurrence of an ineffective electrocatalyst in the cathode side due to the strong O=O bonding and the decomposition of H_2O_2 [7]. H_2O_2 is an undesirable by-product of the ORR, where two electrons are indirectly transferred from O_2 , indicating lower oxygen utilization [8]. Furthermore, H_2O_2 has strong oxidation activity, leading to the corrosion of the catalyst and chemical degradation [7].

Pt and Pt-based materials are state-of-the-art catalysts for the ORR. However, they have seriously hindered applications because of their high cost and limited availability [9]. In addition, Pt possesses poor stability, which is presented by the loss of platinum on the surface area due to (1) corrosion of the carbon support reducing the electrical contact, (2) dissolution and redeposition, and (3) agglomerations; these processes reduce the performance of Pt during fuel cell operations [10]. Among numerous efforts to replace Pt-based materials, fabricating an oxide–oxide heterostructure composite is an effective approach. The combination of two metal oxides as cocatalysts enables ORR kinetics and covalent electron transfer, owing to the interphase ligand effect between them [11]. In addition, the oxide–oxide composite favors the chemical disproportionation of the H_2O_2 intermediates to generate OH^- and O_2 species during the ORR [12–14].

Cobalt and manganese oxides have good ORR catalytic ability; hence, they are widely studied for ORR catalysis [15–17]. Possessing a spinel structure, the $\text{Co}^{2+}/\text{Co}^{3+}$ redox couple found in tetrahedral and octahedral voids facilitates the formation of defects, resulting in electron transfer [18]. Like cobalt oxide, manganese oxides (Mn_xO_y) are suitable metal oxides for the catalysis of ORRs owing to their various oxidation states, chemical stability, and low cost. Various other metal oxide-based ORR electrocatalysts, such as the oxides of Cu, Fe, Zr, and Sn, have also been investigated, but they showed lower activity than Co or Mn-based catalysts. However, cobalt and manganese oxides have intrinsically low conductivity and particle aggregation, which contribute to hinder their chemical and thermal stability [9]. Therefore, dispersing cobalt and manganese oxides homogeneously on multiwalled carbon nanotubes (MWCNTs) as the conductive substrate is an effective way to overcome the aforementioned problems [19].

Here, we report a nanosized composite that consists of Mn_3O_4 and Co_3O_4 nanoparticles, which were uniformly anchored to MWCNTs via a one-step simple solvothermal method without adding any intermediate substances. The impact of the homogeneous oxide–oxide structure of the composite on catalytic activity was thoroughly investigated. Upon integrating into DUFCs, the $\text{Mn}_3\text{O}_4\text{-Co}_3\text{O}_4/\text{MWCNT}$ composite exhibited highly electrocatalytic properties compared to the corresponding individual components. The achieved power density was relatively low compared to other currently developed devices, but the catalyst's components are inexpensive and abundant. Moreover, there is a promising approach of a simple and efficient synthesis of the catalyst in the present work. Therefore, the DUFC could be applied for simultaneous wastewater treatment as an efficient process of the proper treatment for urea-containing wastewater from domestic and industrial activities at low cost.

2. Materials and Methods

2.1. Preparation of $\text{Mn}_3\text{O}_4\text{-Co}_3\text{O}_4/\text{MWCNT}$ Composite

For the fabrication of $\text{Mn}_3\text{O}_4\text{-Co}_3\text{O}_4/\text{MWCNT}$, 2 mmol $\text{Co}(\text{CH}_3\text{COO})_2 \cdot 4\text{H}_2\text{O}$ (Sigma Aldrich) was dissolved in 100 mL of ethanol, and the mixture was stirred at room temperature for 2 h. Subsequently, the mixture was transferred into a Teflon-lined autoclave for the solvothermal reaction at 150°C for 5 h. The obtained mixture was cooled to room temperature. Next, 80 mg of ox-MWCNTs (acid-treated MWCNT) and 2 mmol $\text{Mn}(\text{CH}_3\text{COOH})_2 \cdot 4\text{H}_2\text{O}$ (Sigma Aldrich) were added, and the mixture was stirred at 85°C for 3 h. The dark brown precipitates were collected via centrifugation and washed with

ethanol and ultrapure water several times. Furthermore, $\text{Co}_3\text{O}_4/\text{MWCNT}$ and $\text{Mn}_3\text{O}_4/\text{MWCNT}$ were synthesized using the same process.

2.2. Material Characterization

The morphology and particle sizes of the composite were observed via field emission scanning electron microscopy (SEM) (FE-SEM, Hitachi S-4200 system, Tokyo, Japan) and transmission electron microscopy (TEM) (HR-TEM, CRYO-ARM200F, JEOL, Massachusetts, USA). A Brunauer–Emmett–Teller (BET) measurement was performed to investigate the specific surface areas of the obtained samples (Autosorb iQ Station 2). The X-ray diffraction (XRD) spectra were recorded using the Panoalytical Empyrean XRD apparatus with Cu 1.8 KW (Cu $k\text{-}\alpha$ 1.54 Å, max 60 kV, and 55 mA) and PIXCEL 3D with a prefix interface Xenon proportional detector (0D point detector).

2.3. Electrochemical Measurements

Rotating ring disk electrode (RRDE) measurements were performed with an RRDE-3A instrument in the SP-240 Bio-Logic SAS mode to evaluate the activities of $\text{Co}_3\text{O}_4/\text{MWCNT}$, $\text{Mn}_3\text{O}_4/\text{MWCNT}$, and $\text{Mn}_3\text{O}_4\text{-Co}_3\text{O}_4/\text{MWCNT}$ in ORR electrocatalysis. For this measurement, a three-electrode cell was used, which consisted of an RRDE, Ag-AgCl/KCl (0.973 V vs. RHE (reversible hydrogen electrode)), and a Pt wire employed as the working, reference, and counter electrodes, respectively. Typically, 10 mg of a prepared catalyst powder was ultrasonically suspended in 1 mL isopropanol and 100 μL of Nafion for 30 min. Subsequently, 10 μL of the resulting slurry was coated on the surface of the RRDE. All measurements, including cyclic voltammetry (CV), chronoamperometry, and linear sweep voltammetry (LSV) were carried out in 1 M KOH at room temperature. The measuring system was purged with O_2 for at least 30 min before measurements. We also analyzed the scan rate at 20 mV s^{-1} between 0.4 and 1.2 V vs. RHE for CV and 0.5 to 1.2 V vs. RHE at rotating speeds ranging from 400 to 2000 rpm for LSV. The commercial Pt/C (Pt 20%, from Premetek) was subjected to the same method as a reference standard.

2.4. Fabrication and Examination of Membrane Electrode Assembly

A single fuel cell was fabricated to evaluate the practical application of the $\text{Mn}_3\text{O}_4\text{-Co}_3\text{O}_4/\text{MWCNT}$ composite using the as-prepared nanostructure as a cathode catalyst and the commercial Ni/C (Ni 20%, from Premetek) as an anode catalyst with Fumasep FAA-3-50 (Fumatech) anion exchange membranes. For this, 50 mg of the as-prepared catalyst (in powder form) and the commercial Ni/C were dispersed in a mixture of 5% Nafion (200 μL) and isopropanol (800 μL), and sonicated for 30 min to form a uniform ink. The catalyst inks (2 mg cm^{-2}) were then loaded onto a 5.0 cm^2 carbon paper. Both electrodes were attached to the membrane electrolyte by hot-pressing for 2 min at 100 °C. The membrane electrode assemblies were examined in a fuel cell station (Scitech Korea Inc., Seoul, Korea). The experiments were performed in a 0.33 M urea/1 M KOH solution fed as an anolyte and wet O_2 as the catholyte at room temperature.

3. Results and Discussion

The two-step synthesis route of the $\text{Mn}_3\text{O}_4\text{-Co}_3\text{O}_4/\text{MWCNT}$ catalyst is shown in Figure 1. The MWCNT was peroxidized with HNO_3 to enrich the epoxy and hydroxyl functional surface groups. Specifically, $\text{Co}_3\text{O}_4/\text{MWCNT}$ was prepared through the hydrolysis reaction of the cobalt-salt precursor and ox-MWCNT in an ethanol solution without any reducing agents under solvothermal treatment at 150 °C. In the ox-MWCNT template, the Co species were coated homogeneously owing to the attractive electrostatic forces and the good solubility of the reduced MWCNT [20]. In the next step, $\text{Mn}(\text{CH}_3\text{COOH})_2$ was added to the intermediate product solution and stirred at 80 °C for 3 h to form Mn_3O_4 nanoparticles over $\text{Co}_3\text{O}_4/\text{MWCNT}$. Thus, the Mn_3O_4 nuclei were homogeneously anchored to the surface of the MWCNTs.

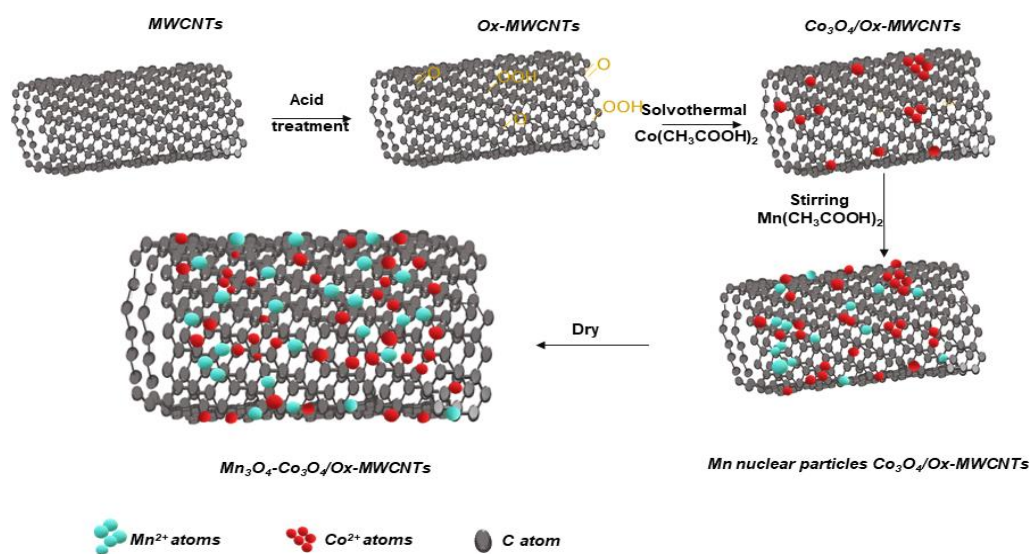


Figure 1. Schematic illustration of the fabrication of Mn_3O_4 - Co_3O_4 /multiwalled carbon nanotubes (MWCNT).

The successful synthesis of manganese–cobalt oxide nanoparticles on the MWCNT composite was confirmed via TEM and SEM, as shown in Figure 2. SEM and TEM images of the obtained products showed that the Mn_3O_4 and Co_3O_4 nanoparticles were homogeneously coated in a high quantity on the surface of the MWCNT template without any aggregation. According to the TEM images shown in Figure 2, the average size of both oxides was small, ranging from 8 to 10 nm, which could be due to the low hydrolysis rate of the precursor [21].

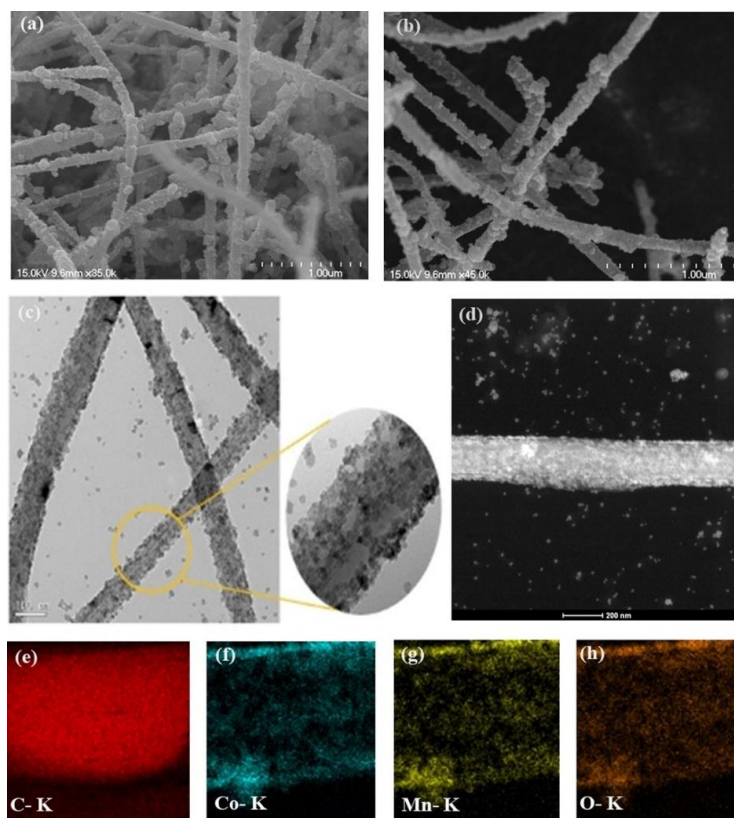


Figure 2. Morphology of the obtained catalyst: (a,b) SEM images of Mn_3O_4 - Co_3O_4 /MWCNT. (c,d) TEM images of Mn_3O_4 - Co_3O_4 /MWCNT. (e–h) Elemental mapping of the Mn_3O_4 - Co_3O_4 /MWCNT catalysts.

The structures and crystallographic phase of the synthesized catalyst were studied through XRD, as shown in Figure 3. For the $\text{Mn}_3\text{O}_4/\text{MWCNT}$ and $\text{Co}_3\text{O}_4/\text{MWCNT}$ catalysts, the diffraction peaks were indexed according to JCPDS 24-0734 and JCPDS 43-1003, respectively. The XRD patterns of the prepared $\text{Mn}_3\text{O}_4\text{-Co}_3\text{O}_4/\text{MWCNT}$ nanoparticles exhibited well-defined peaks at 18.96° (111), 31.09° (220), 36.86° (311), 44.78° (400), 59.11° (511), and 65.28° (440), which were indexed to the Co_3O_4 spinel structure (JCPDS 43-1003). No residual peaks were observed. The individual Co_3O_4 phase had a crystalline structure. In addition, the metal–oxygen–carbon (M–O–C) composite presented a peak at 55° (303), which corresponded to the formed Mn_3O_4 , in reference to JCPDS 27-0734. This observation suggests the formation of Mn_3O_4 in addition to the Co_3O_4 phase in the composite, indicating the presence of a multiphase structure.

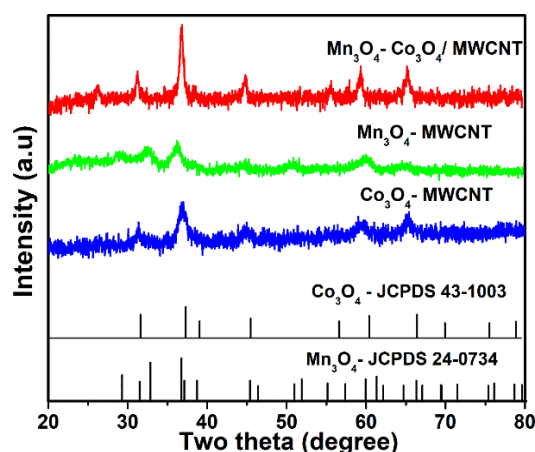


Figure 3. XRD patterns of $\text{Mn}_3\text{O}_4\text{-Co}_3\text{O}_4/\text{MWCNT}$, $\text{Mn}_3\text{O}_4/\text{MWCNT}$, and $\text{Co}_3\text{O}_4/\text{MWCNT}$ samples.

To study the chemical bonding of the synthesized catalysts, we performed X-ray photoelectron spectroscopy (XPS). From the survey spectrum, we confirmed the existence of cobalt, manganese, oxygen, and carbon. The XPS profiles of $\text{Co}2p^{3/2}$ and $\text{Co}2p^{1/2}$ are presented in Figure 4b. The fitting peaks were observed at 780.2 and 795.3 eV for the binding energy at a spin energy gap of 15.1 eV, which further verified the presence of Co_3O_4 in the composite [22]. The presence of Mn_3O_4 was verified by two peaks at 641.8 and 653.4 eV with a separating energy of 11.6 eV, indicating the $\text{Mn}2p^{3/2}$ and $\text{Mn}2p^{1/2}$ spin-orbit states, respectively [23,24]. The $\text{C}1s$ deconvolution spectrum contained three distinguished peaks at 284.5, 286.04, and 282.1 eV, which corresponded to carbon atoms bonded to carbon (C–C), oxygen (C–O), and oxygen in carboxyl groups (O–C=O), respectively [25]. The $\text{O}1s$ spectrum was divided into four distinct peaks, which indicated the formation of oxygen bonds at the interface between the oxides and carbon.

In addition, the $\text{O}1s$ XPS profiles of the individual components $\text{Mn}_3\text{O}_4/\text{MWCNT}$ and $\text{Co}_3\text{O}_4/\text{MWCNT}$ were recorded for reference and are shown in Figure 4e,f. The two peaks at 531.84 and 533.04 eV corresponded to O–C=O and C–O bonding, respectively, which corroborated previously reported results [26,27]. The third peak observed at 529.7 eV was consistent with an M–O bond (M = Co, Mn) [28,29], which is slightly positively shifted. Furthermore, the intensity of this peak decreased compared to that of the individual oxides alone on MWCNTs, demonstrating the coexistence of Mn–O and Co–O in the composite catalysts. The formation of the M–O–C bonding at the interface of the oxide and MWCNTs was also confirmed by comparing the binding energy and intensity in the $\text{O}1s$ of the synthesized catalysts. The characteristic peak at 530.14 eV in the spectrum of the $\text{Mn}_3\text{O}_4\text{-Co}_3\text{O}_4/\text{MWCNT}$ composite was similar to that of $\text{Mn}_3\text{O}_4/\text{MWCNT}$ and $\text{Co}_3\text{O}_4/\text{MWCNT}$. Nonetheless, this peak showed an increased intensity and a slight change in the binding energy, indicating the formation of M–O–C bonding, including Mn–O–C and Co–O–C [30]. In addition, the bonding energy of the well-defined peaks shifted positively from 1 to 3 eV in contrast with that in the M–O bond, which further proved the formation of M–O–C in $\text{Mn}_3\text{O}_4\text{-Co}_3\text{O}_4/\text{MWCNT}$ [20].

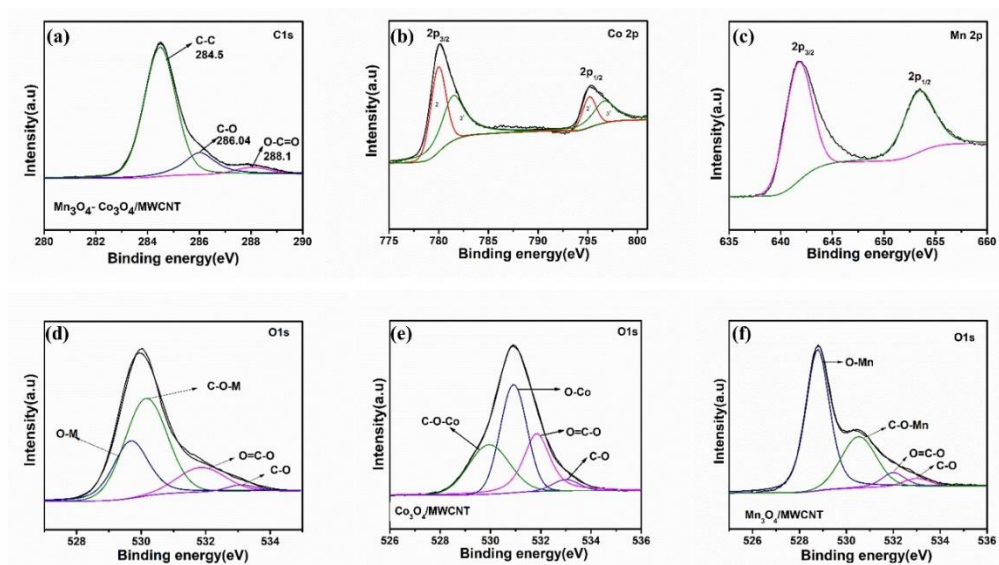


Figure 4. XPS survey spectra of $\text{Mn}_3\text{O}_4\text{-Co}_3\text{O}_4/\text{MWCNT}$. (a) C1s, (b) Co2p, (c) Mn2p, (d) O1s, and (e,f) O1s in individual metal oxides on MWCNTs.

The XPS results demonstrated that the Co_3O_4 and Mn_3O_4 nanoparticles were decorated over the surface of the MWCNTs, and this was highly related to the enhancement of the electrochemical performance. The high concentration of oxygen vacancies could facilitate oxygen adsorption and covalent metal oxide–nanocarbon bonding and enable improved electron transfer across the interface. The specific areas of $\text{Mn}_3\text{O}_4\text{-Co}_3\text{O}_4/\text{MWCNT}$ were $99.82 \text{ m}^2/\text{g}$ as obtained from the BET analysis shown as Figure 5. The large specific surface areas of the synthesized composite could facilitate the adsorption and transportation of O_2 and H_2O during the ORR.

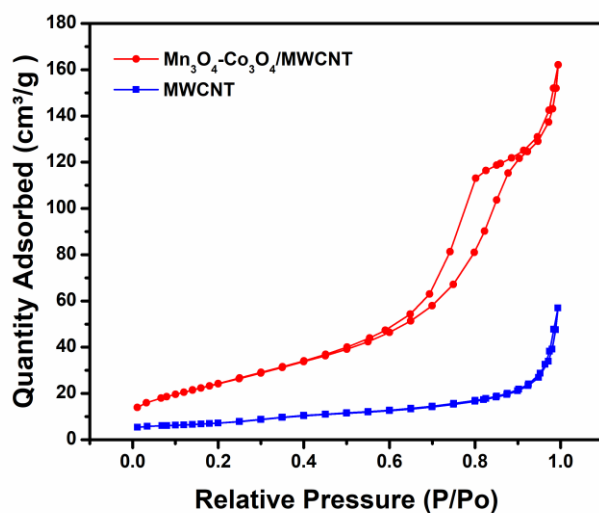


Figure 5. Brunauer–Emmett–Teller (BET) nitrogen adsorption–desorption isotherms of $\text{Mn}_3\text{O}_4\text{-Co}_3\text{O}_4/\text{MWCNT}$ and MWCNT.

To assess the catalytic activity of $\text{Mn}_3\text{O}_4\text{-Co}_3\text{O}_4/\text{MWCNT}$, we evaluated the individual components using commercial Pt/C 20% as a comparative sample via CV on an RRDE in O_2 -saturated 1.0 M KOH. The observed ORR peaks for the obtained sample are depicted in Figure 6. The CV curves of the $\text{Mn}_3\text{O}_4\text{-Co}_3\text{O}_4/\text{MWCNT}$ composite suggest much higher activity than those of Co_3O_4 and Mn_3O_4 . Additionally, the curves were compared with those of Pt/C. The reduction peaks of all synthesized samples had the same position peak (0.7 V vs. RHE), but the diffusion limiting current density

followed this sequence: $\text{Mn}_3\text{O}_4\text{-Co}_3\text{O}_4/\text{MWCNT} > \text{Co}_3\text{O}_4/\text{MWCNT} > \text{Mn}_3\text{O}_4/\text{MWCNT}$. The reduction peak reached approximately 3.55 mA cm^{-2} for the $\text{Mn}_3\text{O}_4\text{-Co}_3\text{O}_4/\text{MWCNT}$ composite and was approximately 1.3 times higher than that of Co_3O_4 (2.54 mA cm^{-2}) and Mn_3O_4 (2.49 mA cm^{-2}), indicating that the combination of metal oxides can significantly improve the ORR activity. In addition, the current density of the $\text{Mn}_3\text{O}_4\text{-Co}_3\text{O}_4/\text{MWCNT}$ composite was close to that of Pt/C; however, the more positive the peak potential was (0.7 V), the more positively shifted the onset potential (0.85 V) was, as shown in Figure 6b. Thus, the $\text{Mn}_3\text{O}_4\text{-Co}_3\text{O}_4/\text{MWCNT}$ composite was an active electrocatalyst for the ORR.

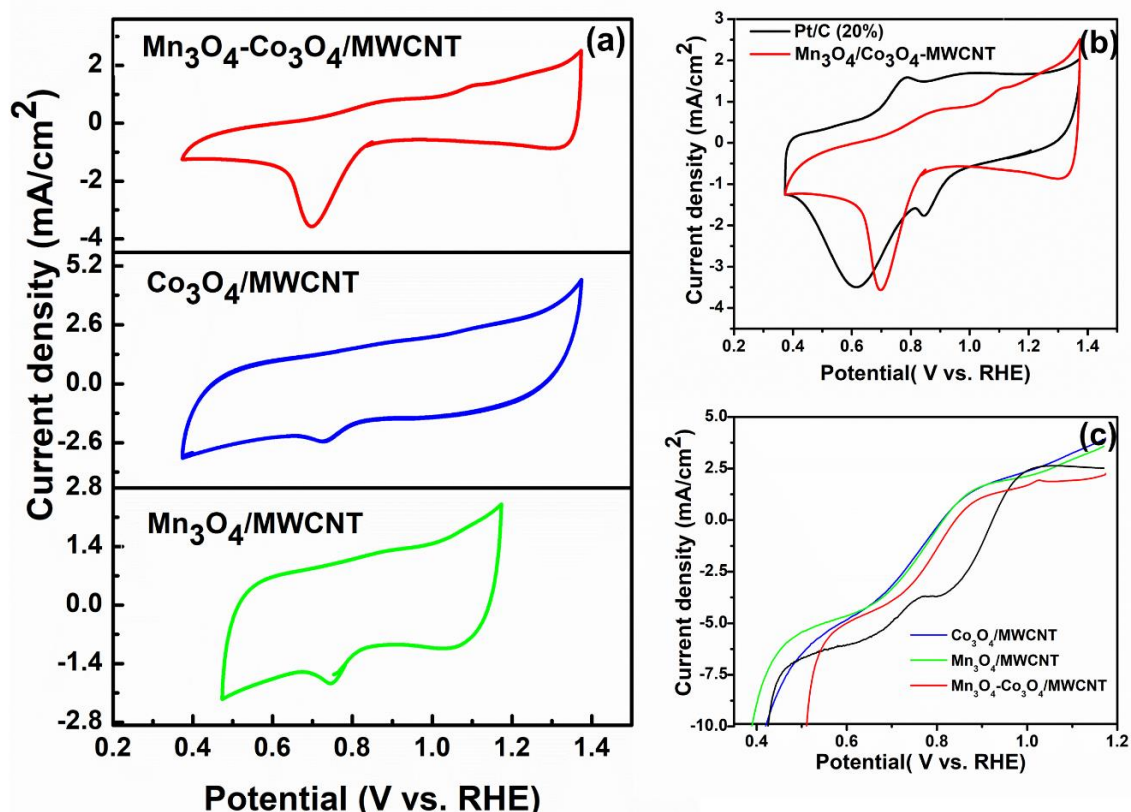


Figure 6. Cyclic voltammetry (CV) curves of the $\text{Mn}_3\text{O}_4\text{-Co}_3\text{O}_4/\text{MWCNT}$ electrocatalyst, (a) individual components, and (b) Pt/C reference for comparison. Measurements were performed in an O_2 -saturated 1.0 M KOH electrolyte. (c) Polarization oxygen reduction reaction (ORR) curves of all as-prepared catalysts at 1600 rpm in 1.0 M KOH.

For comparison, the polarization curves for the ORR were also recorded in a 1 M KOH solution at 1600 rpm, as shown in Figure 6c. The electrocatalytic activity of the composite catalyst was higher than the activities of its individual components and approximately equal to that of the commercial Pt/C owing to their higher current density and positive half-wave potential. The results illustrated that the onset potential of the composite (0.87 V) was higher than that of Mn_3O_4 and Co_3O_4 (0.84 V) and lower than that of the Pt/C catalyst (0.97 V). The current density on the composite was 4.97 mA cm^{-2} at 0.6 V, which was higher than that of Co_3O_4 (4.70 mA cm^{-2}) and Mn_3O_4 (4.53 mA cm^{-2}) and similar to that of Pt/C. To gain insight into the kinetics of the ORR, the LSV of $\text{Mn}_3\text{O}_4\text{-Co}_3\text{O}_4/\text{MWCNT}$ was recorded in O_2 -saturated 1.0 M KOH at different rotating rates. As shown in Figure 7a, the polarization curves suggested that the measured current intensity increased with the high-speed rotation rates because of the enhanced diffusion. Based on the diffusion in the kinetically limited regions, we used the Koutecky–Levich (K–L) plot to determine the electron transfer number. The K–L equation is [31]:

$$\frac{1}{J} = \frac{1}{J_L} + \frac{1}{J_k} = \frac{1}{B\omega^{1/2}} + \frac{1}{J_k} \quad (1)$$

$$B = 0.62nFC_0D_0^{2/3} \nu^{-1/6} \quad (2)$$

where J is the measured current density; J_k is the kinetic current density; B is the Levich constant or proportionality coefficient, which could be determined from the slope of the K–L plot; ω is the electrode rotating rate, $F = 96485 \text{ C mol}^{-1}$; ν is the kinematic viscosity of the electrolyte ($\nu = 0.01 \text{ cm}^2 \text{ s}^{-1}$); $C_0 = 7.8 \times 10^{-7} \text{ mol cm}^{-3}$ is the concentration of O_2 in the electrolyte; and $D_0 = 1.8 \times 10^{-5} \text{ m}^2 \text{ s}^{-1}$ is the diffusion coefficient of O_2 in 1.0 M KOH. The electron transfer number was calculated using Equations (1) and (2) reaching up to 3.71 electrons, indicating a four-electron oxygen reduction pathway.

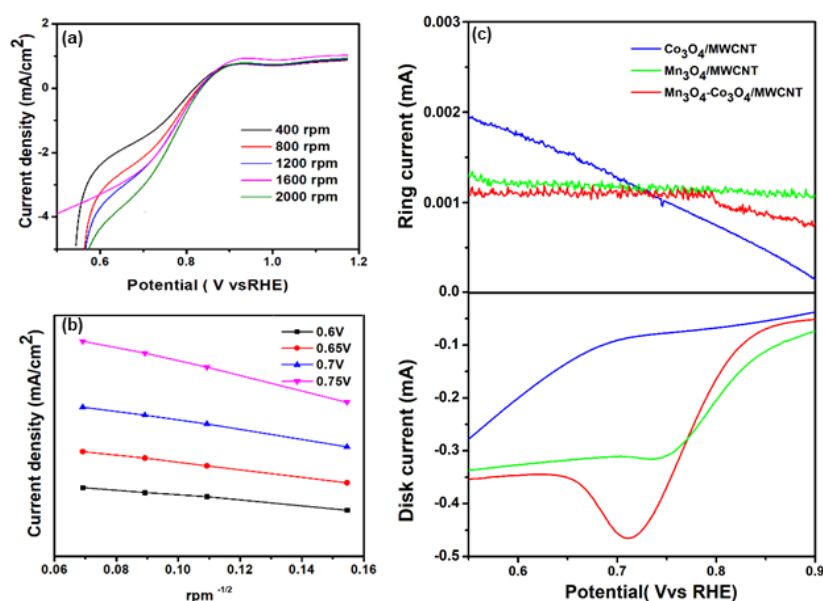


Figure 7. (a) Ring disk electrode (RDE) curves of $\text{Mn}_3\text{O}_4\text{-Co}_3\text{O}_4/\text{MWCNT}$ at different rotating speeds. (b) Koutecky–Levich (K–L) plots obtained from the RDE measurements. (c) Polarization curves for the ORR on different electrocatalysts in a O_2 -saturated 1.0 M KOH aqueous solution at 1600 rpm.

To gain further insight into the activities of the catalysts in the ORR, we investigated the reaction kinetics at a rotation rate of 1600 rpm. During the experiment, the disk potential was scanned at 0.55–0.9 V vs. RHE, while the ring potential was maintained at 0.627 V. As shown in Figure 7c, both ring and disk currents increased rapidly because the oxygen supply was sufficient on the surface of the working electrode to enhance the acceleration rate of the ORR. $\text{Co}_3\text{O}_4/\text{MWCNT}$ and $\text{Mn}_3\text{O}_4/\text{MWCNT}$ had very similar disk currents, whereas the composite catalyst exhibited a higher ring current. The onset potential and current density peaked at 0.855 V and 0.465 mA, which were higher than those of the other catalysts. The half-wave potential and diffusion-limited current increased in the following order: $\text{Co}_3\text{O}_4/\text{MWCNT} \leq \text{Mn}_3\text{O}_4/\text{MWCNT} < \text{Mn}_3\text{O}_4\text{-Co}_3\text{O}_4/\text{MWCNT}$, illustrating the increase in the ORR activity.

In addition, the electron transfer number and peroxide percentages were obtained as a function of both disk and ring currents using the following equation from the RRDE technique [31].

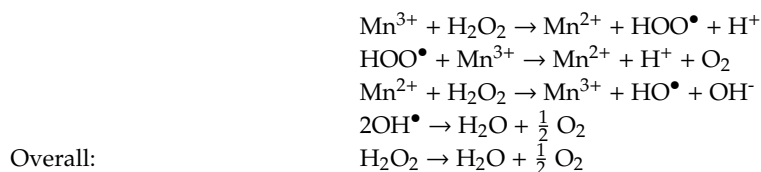
$$n = \frac{4I_D}{I_D + I_R \cdot N} \quad (3)$$

$$\% \text{H}_2\text{O}_2 = \frac{100nI_R}{2I_D N} \quad (4)$$

where I_D and I_R are the currents at the disk and ring electrodes, respectively, and $N = 0.317 (I_D/I_R)$ is the RRDE collection efficiency. For the as-prepared catalysts $\text{Mn}_3\text{O}_4\text{-Co}_3\text{O}_4/\text{MWCNT}$, $\text{Co}_3\text{O}_4/\text{MWCNT}$, and $\text{Mn}_3\text{O}_4/\text{MWCNT}$, the $\chi \text{ H}_2\text{O}_2$ were 2%, 4.46%, and 2.5%, and the n values were 3.96, 3.91, and 3.94, respectively. These values were similar to those obtained from the K–L plot, but a small difference

remained due to the calculation process. However, the results presented a preference for a direct four-electron reduction pathway. $\text{Mn}_3\text{O}_4\text{-Co}_3\text{O}_4/\text{MWCNT}$ showed the highest n value (3.96) and the lowest χ H_2O_2 (2%), which proved its superior electrochemical activity compared to $\text{Co}_3\text{O}_4/\text{MWCNT}$ and $\text{Mn}_3\text{O}_4/\text{MWCNT}$.

The improved performance (higher electron transfer and lower ring current) of the $\text{Mn}_3\text{O}_4\text{-Co}_3\text{O}_4/\text{MWCNT}$ catalyst can be attributed to the following reasons (Figure 8). First, the uniformity of the Co_3O_4 and Mn_3O_4 metal oxides decorated on the surface of the MWCNTs enabled C-O-M covalent bonding at the interface [32–35]. The fine decoration of the $\text{Mn}_3\text{O}_4\text{-Co}_3\text{O}_4$ nanoparticles contributed to this activation [36]:



In this process, a trace amount of the H_2O_2 intermediate undergoes chemical disproportionation to generate O_2 species, which can be used as reactants for a further ORR [37]. Similarly, OH^- is produced by catalyzing the decomposition of H_2O_2 with Co_3O_4 nanoparticles [34]. In addition, the Co^{3+} species of Co_3O_4 provide a surface electronic state, which carries electrons from bulk oxides to produce an excited cationic state, facilitating the ORR [37]. Moreover, the uniform metal oxides decorated on MWCNTs confine agglomerations, which contribute to the active surface areas. Additionally, this process can enhance the electronic conductivity due to the efficient generation of ions in the alkaline media [38,39].

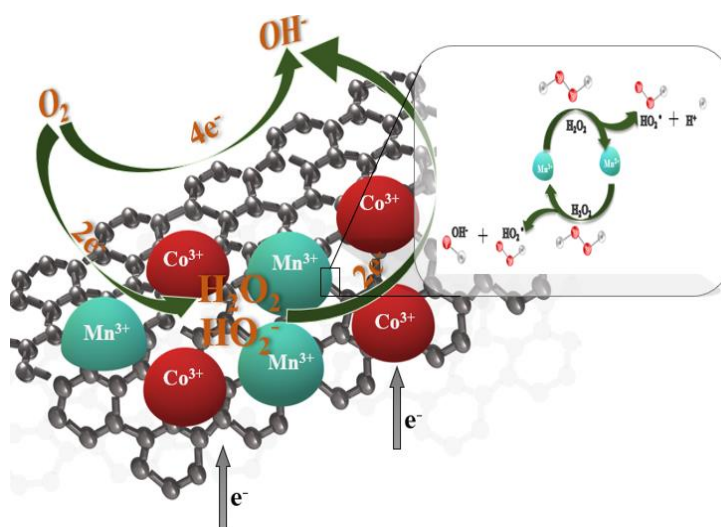


Figure 8. Schematic diagram of the ORR on $\text{Mn}_3\text{O}_4\text{-Co}_3\text{O}_4/\text{MWCNT}$.

Fuel tolerance and stability are vital characteristics of a high-performing ORR catalyst. Urea crossover tests were performed in a 1.0 M KOH solution containing 5 mL of 0.33 M urea, as shown in Figure 9a,b. The current density immediately decreased by 43% at 0.7 V for Pt/C after injecting the urea solution, whereas that of the $\text{Mn}_3\text{O}_4\text{-Co}_3\text{O}_4/\text{MWCNT}$ catalyst showed a minor decrease and retained 92% of its initial value. This behavior demonstrated that Pt/C could not withstand the urea crossover. With regard to the long-time durability of the catalysts, the voltammograms showed high stability of $\text{Mn}_3\text{O}_4\text{-Co}_3\text{O}_4/\text{MWCNT}$ with no distinct current change; the initial limiting current density was 0.672 V (vs. RHE). Figure 9c,d presents the chronoamperometric responses of the commercial Pt/C and the as-prepared $\text{Mn}_3\text{O}_4\text{-Co}_3\text{O}_4/\text{MWCNT}$ catalyst at a rotation rate of 1000 rpm in a 1M KOH

solution for 5000 s. The commercial Pt/C dropped approximately 10% of its initial current due to the formation of Pt hydroxide on its surface. It is clear that $\text{Mn}_3\text{O}_4\text{-Co}_3\text{O}_4/\text{MWCNT}$ underwent an inconsiderable decrease and remained stable at 97% of its initial current after 5000 s. The obtained results demonstrate that $\text{Mn}_3\text{O}_4\text{-Co}_3\text{O}_4/\text{MWCNT}$ has a superior long-term stability in comparison with commercial Pt/C. [39]. All chronoamperometric responses demonstrate that the Mn–Co oxide composite possessed high durability and favorable kinetics. Therefore, the composite can be used effectively as a cathode catalyst in an alkaline fuel cell.

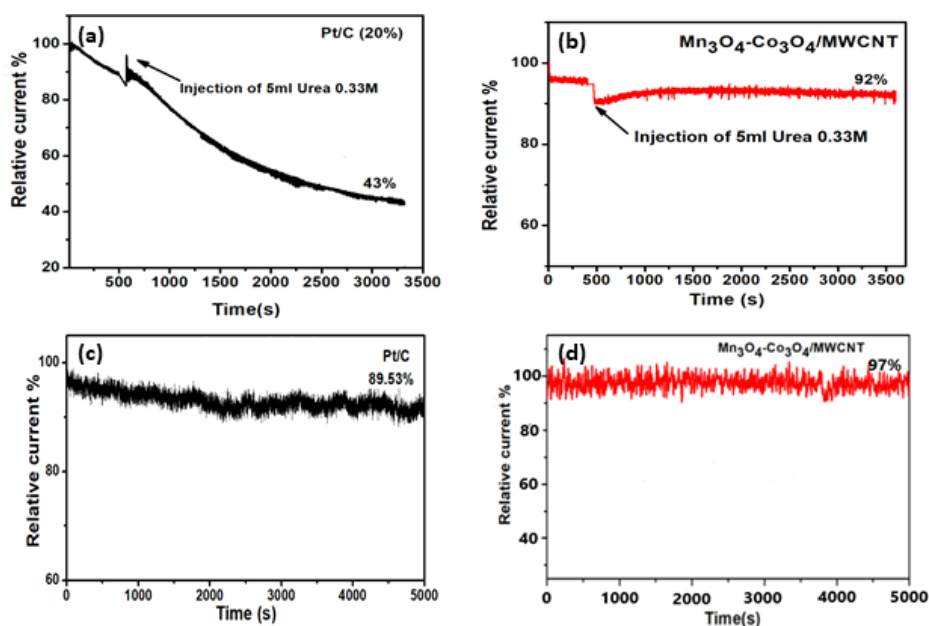


Figure 9. Chronoamperometric curves of (a,c) commercial Pt/C and (b,d) $\text{Mn}_3\text{O}_4\text{-Co}_3\text{O}_4/\text{MWCNT}$ obtained at a rotation rate of 1600 rpm in O_2 -saturated 1 M KOH and after injecting 5 mL of 0.33 M urea in the electrolyte solution at 500 s.

Furthermore, we evaluated the cell performance of the prepared sample used as a catholyte in DUFC. Figure 10 shows the polarization and power density curves of $\text{Mn}_3\text{O}_4\text{-Co}_3\text{O}_4/\text{MWCNT}$ at room temperature. A current density of 2.13 mA cm^{-2} and a maximum power density of $0.4226 \text{ mW cm}^{-2}$ at 50°C were obtained.

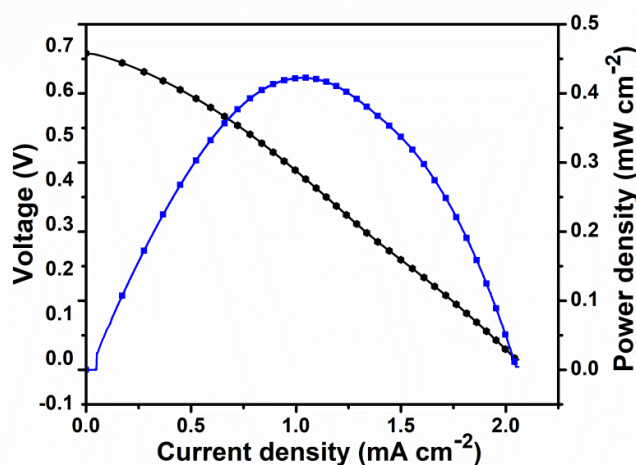


Figure 10. Performance of urea/ O_2 fuel cell using Ni/C, FAAs, and $\text{Mn}_3\text{O}_4\text{-Co}_3\text{O}_4/\text{MWCNT}$ as anode, membrane, and cathode materials, respectively.

4. Conclusions

We prepared a $\text{Mn}_3\text{O}_4\text{-Co}_3\text{O}_4/\text{MWCNT}$ nanocomposite with high catalytic performance in the ORR by growing Co_3O_4 and Mn_3O_4 nanoparticles on the surface of MWCNTs via a solvothermal method without adding any reducing agents. The electrochemical evaluation showed that the composite presented both improved activity compared to the individual components and stability in an alkaline solution comparable to that of commercial Pt/C. Moreover, the $\text{Mn}_3\text{O}_4\text{-Co}_3\text{O}_4/\text{MWCNT}$ catalyst could tolerate urea poisoning and did not degrade in the long term. Thus, $\text{Mn}_3\text{O}_4\text{-Co}_3\text{O}_4/\text{MWCNT}$ can be considered as a low-cost, environmentally friendly, and efficient catalyst for DUFs.

Author Contributions: Conceptualization, T.N.T.P.; methodology, T.N.T.P. and Y.S.Y.; investigation, T.N.T.P.; writing—original draft preparation, T.N.T.P.; writing—review & editing, T.N.T.P. and Y.S.Y.; supervision, Y.S.Y. All authors have read and agreed to the published version of the manuscript.

Funding: This research was funded by Ministry of Knowledge Economy of the Korean Government grant number 20194030202440.

Acknowledgments: This research was supported by the Advanced Track for Hydrogen Production from Renewable Energy Resources, Hydrogen Storage, and Integrated System Engineering Technology of the Korea Institute of Energy Technology Evaluation and Planning (KETEP) grant funded by the Ministry of Knowledge Economy of the Korean Government (No. 20194030202440).

Conflicts of Interest: There are no conflict of interest to declare.

References

1. Rollinson, A.N.; Jones, J.; Dupont, V.; Twigg, M.V. Urea as a hydrogen carrier: A perspective on its potential for safe, sustainable and long-term energy supply. *Energy Environ. Sci.* **2011**, *4*, 1216–1224. [[CrossRef](#)]
2. Rollinson, A.N.; Rickett, G.L.; Lea-Langton, A.; Dupont, V.; Twigg, M.V. Hydrogen from urea-water and ammonia-water solutions. *Appl. Catal. B* **2011**, *106*, 304–315. [[CrossRef](#)]
3. Zhan, S.; Zhou, Z.; Liu, M.; Jiao, Y.; Wang, H. 3D NiO nanowalls grown on Ni foam for highly efficient electro-oxidation of urea. *Catal. Today* **2019**, *327*, 398–404. [[CrossRef](#)]
4. Yousef, A.; El-Newehy, M.H.; Al-Deyab, S.S.; Barakat, N.A.M. Facile synthesis of Ni-decorated multi-layers graphene sheets as effective anode for direct urea fuel cells. *Arab. J. Chem.* **2017**, *10*, 811–822. [[CrossRef](#)]
5. Xu, W.; Wu, Z.; Tao, S. Urea-Based Fuel Cells and Electrocatalysts for Urea Oxidation. *Energy Technol.* **2016**, *4*, 1329–1337. [[CrossRef](#)]
6. Lan, R.; Tao, S.; Irvine, J.T.S. A direct urea fuel cell—Power from fertiliser and waste. *Energy Environ. Sci.* **2010**, *3*, 438–441. [[CrossRef](#)]
7. Sayed, E.T.; Eisa, T.; Mohamed, H.O.; Abdelkareem, M.A.; Allagui, A.; Alawadhi, H.; Chae, K.J. Direct urea fuel cells: Challenges and opportunities. *J. Power Sources* **2019**, *417*, 159–175. [[CrossRef](#)]
8. Cao, D.; Chen, D.; Lan, J.; Wang, G. An alkaline direct $\text{NaBH}_4\text{-H}_2\text{O}_2$ fuel cell with high power density. *J. Power Sources* **2009**, *190*, 346–350. [[CrossRef](#)]
9. Xia, W.; Mahmood, A.; Liang, Z.; Zou, R.; Guo, S. Earth-Abundant Nanomaterials for Oxygen Reduction. *Angew. Chem.* **2016**, *55*, 2650–2676. [[CrossRef](#)] [[PubMed](#)]
10. Chen, Z.; Waje, M.; Li, W.; Yan, Y. Supportless Pt and PtPd nanotubes as electrocatalysts for oxygen-reduction reactions. *Angew. Chem.* **2007**, *46*, 4060–4063. [[CrossRef](#)] [[PubMed](#)]
11. Li, K.; Zhang, R.; Gao, R.; Shen, G.Q.; Pan, L.; Yao, Y.; Yu, K.; Zhang, X.; Zou, J.J. Metal-defected spinel $\text{Mn}_x\text{Co}_{3-x}\text{O}_4$ with octahedral Mn-enriched surface for highly efficient oxygen reduction reaction. *Appl. Catal. B* **2019**, *244*, 536–545. [[CrossRef](#)]
12. Du, G.; Liu, X.; Zong, Y.; Hor, T.S.A.; Yu, A.; Liu, Z. Co_3O_4 nanoparticle-modified MnO_2 nanotube bifunctional oxygen cathode catalysts for rechargeable zinc-air batteries. *Nanoscale* **2013**, *5*, 4657–4661. [[CrossRef](#)] [[PubMed](#)]
13. Wang, Y.; Ma, X.; Lu, L.; He, Y.; Qi, X.; Deng, Y. Carbon supported $\text{MnO}_x\text{-Co}_3\text{O}_4$ as cathode catalyst for oxygen reduction reaction in alkaline media. *Int. J. Hydrog. Energy* **2013**, *38*, 13611–13616. [[CrossRef](#)]
14. Senthilkumar, N.; Gnana kumar, G.; Manthiram, A. 3D Hierarchical Core–Shell Nanostructured Arrays on Carbon Fibers as Catalysts for Direct Urea Fuel Cells. *Adv. Energy Mater.* **2018**, *8*, 1702207. [[CrossRef](#)]

15. Liang, Y.; Li, Y.; Wang, H.; Zhou, J.; Wang, J.; Regier, T.; Dai, H. Co₃O₄ nanocrystals on graphene as a synergistic catalyst for oxygen reduction reaction. *Nat. Mater.* **2011**, *10*, 780–786. [[CrossRef](#)]
16. Chai, H.; Xu, J.; Han, J.; Su, Y.; Sun, Z.; Jia, D.; Zhou, W. Facile synthesis of Mn₃O₄-rGO hybrid materials for the high-performance electrocatalytic reduction of oxygen. *J. Colloid Interface Sci.* **2017**, *488*, 251–257. [[CrossRef](#)]
17. Huang, D.; Zhang, B.; Li, S.; Wang, M.; Shen, Y. Mn₃O₄/Carbon Nanotube Nanocomposites as Electrocatalysts for the Oxygen Reduction Reaction in Alkaline Solution. *ChemElectroChem* **2014**, *1*, 1531–1536. [[CrossRef](#)]
18. Akbari, A.; Amini, M.; Tarassoli, A.; Eftekhari-Sis, B.; Ghasemian, N.; Jabbari, E. Transition metal oxide nanoparticles as efficient catalysts in oxidation reactions. *Nano-Struct. Nano-Objects* **2018**, *14*, 19–48. [[CrossRef](#)]
19. Thangasamy, P.; Selvakumar, K.; Sathish, M.; Kumar, S.M.S.; Thangamuthu, R. Anchoring of ultrafine Co₃O₄ nanoparticles on MWCNTs using supercritical fluid processing and its performance evaluation towards electrocatalytic oxygen reduction reaction. *Catal. Sci. Technol.* **2017**, *7*, 1227–1234. [[CrossRef](#)]
20. Liu, J.; Liu, J.; Song, W.; Wang, F.; Song, Y. The role of electronic interaction in the use of Ag and Mn₃O₄ hybrid nanocrystals covalently coupled with carbon as advanced oxygen reduction electrocatalysts. *J. Mater. Chem. A* **2014**, *2*, 17477–17488. [[CrossRef](#)]
21. Ghosh Chaudhuri, R.; Paria, S. Core/shell nanoparticles: Classes, properties, synthesis mechanisms, characterization, and applications. *Chem. Rev.* **2012**, *112*, 2373–2433. [[CrossRef](#)] [[PubMed](#)]
22. Menezes, P.W.; Indra, A.; González-Flores, D.; Sahraie, N.R.; Zaharieva, I.; Schwarze, M.; Strasser, P.; Dau, H.; Driess, M. High-Performance Oxygen Redox Catalysis with Multifunctional Cobalt Oxide Nanochains: Morphology-Dependent Activity. *ACS Catal.* **2015**, *5*, 2017–2027. [[CrossRef](#)]
23. Zhao, T.; Gadipelli, S.; He, G.; Ward, M.J.; Do, D.; Zhang, P.; Guo, Z. Tunable Bifunctional Activity of Mn_xCo_{3-x}O₄ Nanocrystals Decorated on Carbon Nanotubes for Oxygen Electrocatalysis. *ChemSusChem* **2018**, *11*, 1248. [[CrossRef](#)]
24. Duan, J.; Zheng, Y.; Chen, S.; Tang, Y.; Jaroniec, M.; Qiao, S. Mesoporous hybrid material composed of Mn₃O₄ nanoparticles on nitrogen-doped graphene for highly efficient oxygen reduction reaction. *Chem. Commun.* **2013**, *49*, 7705–7707. [[CrossRef](#)] [[PubMed](#)]
25. Xiao, J.; Wan, L.; Wang, X.; Kuang, Q.; Dong, S.; Xiao, F.; Wang, S. Mesoporous Mn₃O₄-CoO core-shell spheres wrapped by carbon nanotubes: A high performance catalyst for the oxygen reduction reaction and CO oxidation. *J. Mater. Chem. A* **2014**, *2*, 3794–3800. [[CrossRef](#)]
26. Jiang, Z.; Jiang, Z.J.; Maiyalagan, T.; Manthiram, A. Cobalt oxide-coated N- and B-doped graphene hollow spheres as bifunctional electrocatalysts for oxygen reduction and oxygen evolution reactions. *J. Mater. Chem. A* **2016**, *4*, 5877–5889. [[CrossRef](#)]
27. Su, Y.; Zhu, Y.; Jiang, H.; Shen, J.; Yang, X.; Zou, W.; Chen, J.; Li, C. Cobalt nanoparticles embedded in N-doped carbon as an efficient bifunctional electrocatalyst for oxygen reduction and evolution reactions. *Nanoscale* **2014**, *6*, 15080–15089. [[CrossRef](#)]
28. Duan, J.; Chen, S.; Dai, S.; Qiao, S.Z. Shape control of Mn₃O₄ nanoparticles on nitrogen-doped graphene for enhanced oxygen reduction activity. *Adv. Funct. Mater.* **2014**, *24*, 2072–2078. [[CrossRef](#)]
29. Ma, T.Y.; Zheng, Y.; Dai, S.; Jaroniec, M.; Qiao, S.Z. Mesoporous MnCo₂O₄ with abundant oxygen vacancy defects as high-performance oxygen reduction catalysts. *J. Mater. Chem. A* **2014**, *2*, 8676–8682. [[CrossRef](#)]
30. Dai, L.; Liu, M.; Song, Y.; Liu, J.; Wang, F. Mn₃O₄-decorated Co₃O₄ nanoparticles supported on graphene oxide: Dual electrocatalyst system for oxygen reduction reaction in alkaline medium. *Nano Energy* **2016**, *27*, 185–195. [[CrossRef](#)]
31. Paulus, U.A.; Schmidt, T.J.; Gasteiger, H.A.; Behm, R.J. Oxygen reduction on a high-surface area Pt/Vulcan carbon catalyst: A thin-film rotating ring-disk electrode study. *J. Electroanal. Chem.* **2001**, *495*, 134–145. [[CrossRef](#)]
32. Xin, S.; Guo, Y.G.; Wan, L.J. Nanocarbon networks for advanced rechargeable lithium batteries. *Acc. Chem. Res.* **2012**, *45*, 1759–1769. [[CrossRef](#)] [[PubMed](#)]
33. Sonkar, P.K.; Prakash, K.; Yadav, M.; Ganesan, V.; Sankar, M.; Gupta, R.; Yadav, D.K. Co(II)-porphyrin-decorated carbon nanotubes as catalysts for oxygen reduction reactions: An approach for fuel cell improvement. *J. Mater. Chem. A* **2017**, *5*, 6263–6276. [[CrossRef](#)]
34. Mu, J.; Wang, Y.; Zhao, M.; Zhang, L. Intrinsic peroxidase-like activity and catalase-like activity of Co₃O₄ nanoparticles. *Chem. Commun.* **2012**, *48*, 2540–2542. [[CrossRef](#)]

35. Petlicki, J.; Palusova, D.; Van De Ven, T.G.M. Physicochemical aspects of catalytic decomposition of hydrogen peroxide by manganese compounds. *Ind. Eng. Chem. Res.* **2005**, *44*, 2002–2010. [[CrossRef](#)]
36. Rhadfi, T.; Piquemal, J.Y.; Sicard, L.; Herbst, F.; Briot, E.; Benedetti, M.; Atlamsani, A. Polyol-made Mn_3O_4 nanocrystals as efficient Fenton-like catalysts. *Appl. Catal. A* **2010**, *386*, 132–139. [[CrossRef](#)]
37. Valim, R.B.; Santos, M.C.; Lanza, M.R.V.; MacHado, S.A.S.; Lima, F.H.B.; Calegario, M.L. Oxygen reduction reaction catalyzed by ϵ - MnO_2 : Influence of the crystalline structure on the reaction mechanism. *Electrochim. Acta* **2012**, *85*, 423–431. [[CrossRef](#)]
38. Xu, J.; Gao, P.; Zhao, T.S. Non-precious Co_3O_4 nano-rod electrocatalyst for oxygen reduction reaction in anion-exchange membrane fuel cells. *Energy Environ. Sci.* **2012**, *5*, 5333–5339. [[CrossRef](#)]
39. Greeley, J.; Stephens, I.E.L.; Bondarenko, A.S.; Johansson, T.P.; Hansen, H.A.; Jaramillo, T.F.; Rossmeisl, J.; Chorkendorff, I.; Nørskov, J.K. Alloys of platinum and early transition metals as oxygen reduction electrocatalysts. *Nat. Chem.* **2009**, *1*, 552–556. [[CrossRef](#)]



© 2020 by the authors. Licensee MDPI, Basel, Switzerland. This article is an open access article distributed under the terms and conditions of the Creative Commons Attribution (CC BY) license (<http://creativecommons.org/licenses/by/4.0/>).